Mechanism for deep crustal seismicity: Insight from modeling of deformation process at the Main Ethiopian Rift

Ameha A. Muluneh[1], Sascha Brune[2,3], Finnigan Illsley-Kemp[4], Giacomo Corti[5], Derek Keir[6,7], Anne Glerum[2], Tesfaye Kidane[1,8], Jim Mori[9]

[1]School of Earth Sciences, Addis Ababa University, Addis Ababa, Ethiopia

[2]Helmholtz Centre Potsdam, GFZ German Research Centre for Geosciences, Potsdam, Germany

[3]Institute of Geosciences, University of Potsdam, Potsdam-Golm, Germany

[4]Institute of Geophysics, Victoria University of Wellington, Wellington, New Zealand

[5]CNR, Istituto di Geoscienze e Georisorse, UOS Firenze, Firenze, Italy

[6]School of Ocean and Earth Science, University of Southampton, Southampton, UK

[7]Dipartimento di Scienze della Terra, Università degli Studi di Firenze, Florence, Italy

[8]School of Agriculture, Earth and Environmental Sciences, University of KuwaZulu Natal, Durban, South Africa

[9]Disaster Prevention and Research Institute, Kyoto University, Kyoto, Japan

Key Points:

- Results from numerical modeling of lithospheric extension and crustal stress state are compared with depth distribution of seismicity.
- We reproduce the timing and locus of basin-ward localisation, and the bimodal depth distribution of earthquakes.
- Bimodal distribution of seismic moment release in MER is controlled by the rheology of the crust.

Corresponding author: Ameha Muluneh, amugeol@gmail.com;ameha.atnafu@aau.edu.et

This article has been accepted for publication and undergone full peer review but has not been through the copyediting, typesetting, pagination and proofreading process which may lead to differences between this version and the Version of Record. Please cite this article as doi: 10.1029/2020GC008935

Abstract

We combine numerical modeling of lithospheric extension with analysis of seismic moment release and earthquake b-value in order to elucidate the mechanism for deep crustal seismicity and seismic swarms in the Main Ethiopian Rift (MER). We run 2D numerical simulations of lithospheric deformation calibrated by appropriate rheology and extensional history of the MER to simulate migration of deformation from mid-Miocene border faults to ∼30 km wide zone of Pliocene to recent rift floor faults. While the highest strain rate is localized in a narrow zone within the rift axis, brittle strain has been accumulated in a wide region of the rift. The magnitude of deviatoric stress shows strong variation with depth. The uppermost crust deforms with maximum stress of 80 MPa, at 8-14 km depth stress sharply decreases to 10 MPa and then increases to a maximum of 160 MPa at ∼18 km depth. These 2 peaks at which the crust deforms with maximum stress of 80 MPa or above correspond to peaks in the seismic moment release. Correspondingly, the drop in stress at 8-14 km correlates to a low in seismic moment release. At this depth range, the crust is weaker and deformation is mainly accommodated in a ductile manner. We therefore see a good correlation between depths at which the crust is strong and elevated seismic deformation, while regions where the crust is weaker deform more aseismically. Overall the bimodal depth distribution of seismic moment release is best explained by rheology of the deforming crust.

Plain language summary

Combined analysis of a numerical modeling study on how the Earth extends and deforms and earthquake depth distribution helps to understand the controlling mechanism of the number and magnitude of earthquakes occurring in the Earth. In order to do so, we run models that simulate opening of the Main Ethiopian rift (MER) and compare the results with earthquake depth data from the region. Our model successfully explains the present day deformation style in the MER with deformation concentrating within ∼30 km wide segments in the rift floor, a similar observation to previous results using geophysical surveys. Our integrated analysis shows that at depth shallower than 8 km, there is a maximum of 80 MPa stress available to deform the crust. This depth coincides with the highest seismic moment release in the crust. Between 8-14 km depth, both the seismic moment and stress significantly decrease, but a large number of small magnitude earthquakes occur. This depth range is also characterized by ductile deformation, con-

trary to faulting which is associated with seismicity. Our study suggests that earthquakes in MER are mainly controlled by the rheology of the crust.

1 Introduction

The depth distribution of seismicity in the East African Rift System (EARS) generally shows earthquakes only in the upper crust, or alternatively a clear bimodal pattern with peaks in the upper crust and then in either the lower crust or upper mantle (e.g., Craig et al., 2011; Yang and Chen, 2010). While the upper crustal earthquakes are consistent with deformation of crust dominated by a quartz-rich composition typical of continents, a range of mechanisms are proposed to explain the deeper earthquakes. For example, Seno and Saito (1994) proposed that lower crustal earthquakes occur due to high pore fluid pressure from fluids migrating from the upper mantle. This mechanism is recently used to explain most of deep crustal seismicity in the Tanzanian and Kenyan rifts (e.g., Lindenfeld et al., 2012). Alternatively in the Tanganyika and Main Ethiopian Rift (MER) (Fig. 1), others propose that deep crustal seismicity is driven by brittle faults penetrating the entire crust (Lavayssière et al., 2019; Lloyd et al., 2018). The tectonic faulting at these depths is enabled by the presence of strong crust, either because the entire lithosphere is anomalously thick and cold, or because the lower crust has a mafic composition and is therefore anomalously strong. The bimodal distribution of earthquakes also suggests that the deviatoric stress in parts of the middle crust must be lower than that of the upper crust and of the deep crust/upper mantle (Yang and Chen, 2010).

In this manuscript we explore the deformation of lithosphere and crustal stress patterns to explain variations in the amount of seismicity in the crust. To this end, we use 2D high-resolution visco-plastic numerical experiments. The model results are then compared with seismic moment release and earthquake b-values.

2 Tectonics of the northern Main Ethiopian Rift

Geodetic (Bendick et al., 2006; Bilham et al., 1999), structural (Kurz et al., 2007) and modeling (Corti, 2008) studies in MER indicate the migration of deformation from border faults to ∼60 km long, 20-30 km wide Quaternary to recent "magmatic segments" within the central rift floor (e.g., Ebinger and Casey, 2001). These magmatic segments are now the locus of active faulting, seismicity and volcanism (Keir et al., 2006). The crust beneath the magmatic segments has higher than normal P-wave velocities (V_p), in-

terpreted as evidence for cooled mafic intrusions (e.g., Daly et al., 2008; Keranen et al., 2004; Mackenzie et al., 2005). The V_p is particularly high at lower crustal depths suggesting the lower crust is heavily intruded (Mackenzie et al., 2005). Thermal metamorphism due to this cooled intrusion makes the surrounding crust strong (Lavecchia et al., 2016; Muluneh et al., 2018) and such crustal strength is required to explain the observed melt chemistry in the MER (Armitage et al., 2018). In addition, the mafic rock type of the intrusions is stronger than the surrounding more felsic continental crust (Beutel et al., 2010).

Analysis of earthquake catalogue puts constraints on the depth distribution of seismicity and seismogenic nature of the crust and mantle. The EAGLE catalogue for 2001-2003 recorded ∼2000 earthquakes (Fig. 2A) with magnitudes M_L less than 4.0 (Keir et al., 2006). This catalogue is the best available so far for the region in terms of accuracy of depth and location of earthquakes. The catalogue has an error of ∼2 km and ∼0.6 km in hypocenter and x, y direction, respectively. Seismicity has a maximum depth of ∼32 km, but most of the earthquakes nucleate at depth of <18 km (Figs. 2B and 2C).

The crustal thickness models from the EAGLE active source experiment using P-wave seismic velocity model show significant variations along and across the MER (e.g., Mackenzie et al., 2005; Maguire et al., 2006). The crust is ∼45 km thick beneath the northwestern plateau and 38 km thick beneath the eastern plateau. In the rift, the crust is >35 km thick in the central MER and thins northwards to ∼28 km in the northern MER. The crust consists of a number of distinct layers, most of which are traceable from the plateaus into the rift. The upper crust is ∼28 km thick beneath the northwestern and eastern plateaus. This layer thins to ∼18 km beneath the northern MER. The lower crust ranges in thickness from 14 km beneath the eastern plateau to ∼10 km beneath the northwestern plateau (e.g., Keranen et al., 2004). Beneath the northern MER, the lower crust has a thickness of <10 km (Keranen et al., 2009; Mackenzie et al., 2005). The base of the crust beneath the northwestern plateau and the rift is underlain by anomalously high velocity layer with a thickness of ∼10 km, which is interpreted as heavily intruded lower crust (e.g., Mackenzie et al., 2005).

3 Numerical model

Previous 3D numerical models of the MER successfully explain magmatic segmentations (Beutel et al., 2010), rift propagation and linkage (Brune et al., 2017; Corti et al., 2019) and kinematic consequences during oblique rifting (Duclaux et al., 2019). In the present study, our main interest is to combine numerical modeling of lithospheric extension with the depth distribution of seismicity.

We follow previous modeling approaches (Brune et al., 2017; Corti et al., 2019) and use rheological and thermal parameters to model the evolution of deformation in the northern MER. We also estimate the deviatoric stress available to drive extension at different crustal depths.

3.1 Governing equations

We construct a 2D box setup using thermo-mechanical finite element code ASPECT v2.0.0-pre (Advanced Solver for Problems in the Earth's ConvecTion, Bangerth et al., 2018; Glerum et al., 2018; Heister et al., 2017; Kronbichler et al., 2012; Rose et al., 2017) to model extension of the MER. Our model is based on previous ASPECT setups aimed at modeling continental rift dynamics (Corti et al., 2019; Glerum et al., 2020; Naliboff et al., 2020). We solve the incompressible flow equations for conservation of momentum (eqn. 1), mass (eqn. 2) and energy (eqn. 3) assuming an infinite Prandtl number:

$$-\nabla \cdot (2\eta \dot{\varepsilon}(\boldsymbol{u})) + \nabla P = \rho \boldsymbol{g}, \tag{1}$$

$$\nabla \cdot \boldsymbol{u} = 0, \tag{2}$$

$$\bar{\rho} C_p \left(\frac{\partial T}{\partial t} + \boldsymbol{u} \cdot \nabla T\right) - \nabla \cdot (\kappa + \nu_h(T)) \nabla T = \bar{\rho} H + 2\eta \left(\dot{\varepsilon}(\mathbf{u})\right) : \left(\dot{\varepsilon}(\mathbf{u})\right) + \alpha T \left(\mathbf{u} \cdot \nabla P\right) \tag{3}$$

where η is viscosity, $\dot{\varepsilon}$ is strain rate tensor, $\boldsymbol{u}$ is velocity vector, P is pressure, ρ is density, $\bar{\rho}$ is adiabatic reference density, $\boldsymbol{g}$ is gravitational acceleration, κ is thermal diffusivity, ν_h is artificial diffusivity, C_p is specific heat capacity and H is heat production. Density, ρ, is given as $\rho_0(1-\alpha(T-T_0))$ where ρ_0 is the reference density, α is thermal diffusivity, T is temperature and T_0 is the reference temperature.

For each compositional field c_i, an additional advection equation (eqn. 4) is introduced to eqns. 1-3. As these equations contain no natural diffusion, artificial diffusivity ν_h is introduced to stabilize advection (Kronbichler et al., 2012)

$$\frac{\partial c_i}{\partial t} + \boldsymbol{u} \cdot \nabla c_i - \nabla \cdot (\nu_h(c_i)) \nabla c_i = 0 \tag{4}$$

3.2 Model setup and boundary conditions

The model geometry comprises a domain of 500×160 km in x-(cross-rift) and y-(depth) directions, respectively (Fig. 3). The resolution of our model varies between 1 km in the region of interest (at depths shallower than 50 km and between 125 and 375 km in x-direction) and 2 km outside this area above 130 km depth. The remaining model region has a resolution of 4 km.

Our modeling approach uses constitutive relationships for viscous and plastic rheology. Viscous flow follows a power-law model for diffusion and dislocation creep (Karato and Wu, 1993) (eqn. 5):

$$\sigma'_{eff} = A^{-1/n} \dot{\varepsilon}_{eff}^{1/n} d^{m/n} \exp(\frac{Q + PV}{nRT}) \tag{5}$$

where A is pre-exponent, n is the power law index, m is the grain size exponent, d is grain size, Q is the activation energy, $\dot{\varepsilon}_{eff}$ is the effective deviatoric strain rate, V is activation volume and R is the gas constant. In case of diffusion creep, n=1 and m>0, while for dislocation creep n>1 and m=0.

We simultaneously apply both the dislocation (η_{disl}) and diffusion (η_{diff}) creeps (van der Berg et al., 1993) for the viscous rheology (eqn. 6)

$$\eta_{comp} = (\frac{1}{\eta_{diff}} + \frac{1}{\eta_{disl}})^{-1} \tag{6}$$

where η_{comp} is composite of both viscous creep mechanisms.

Brittle/plastic rheology is implemented by rescaling the effective viscosity η_{eff}^{pl} in such a way that the stress does not exceed the yield stress σ_y (eqn. 7) derived by the Drucker-Prager yield criterion (eqn. 8).

$$\eta_{eff}^{pl} = \frac{\sigma_y}{2\dot{\epsilon}_{eff}} \tag{7}$$

where σ_y is given by

$$\sigma_y = P \sin\phi + C \cos\phi \tag{8}$$

where P is the total pressure, ϕ is angle of internal friction, and C is the cohesion. When the viscous stress exceeds the plastic yield stress, the effective viscoplastic viscosity will be chosen as the plastic viscosity. Otherwise the composite viscosity is used. The effective viscoplastic viscosity is fixed between lower and upper cut-off values of 10^{19} and 10^{24} Pa s, respectively.

The upper crust is modeled using a wet quartzite flow law (Rutter and Brodie, 2003) and the mafic lower crust and weak seed are represented by wet anorthite (Rybacki et al., 2006). Flow laws of dry and wet olivine (Hirth and Kohlstedt, 2003) represent lithospheric mantle and asthenospheric mantle, respectively. The undeformed crust has a thickness of 38 km, with 25 km and 13 km thick upper and lower crust, respectively. The thickness of these layers is based on geophysical observations from the southeastern plateau (e.g., Keranen et al., 2009). Since the southeastern plateau has not been modified by magmatic underplating, unlike the northwestern margin, the crustal thickness represents the thickness prior to the opening of the MER. The initial lithosphere has a thickness of 120 km based on lithospheric thickness from the undeformed part of Africa (e.g., Fishwick, 2010). We set the horizontal component of velocity on the left and right boundaries to $V_{ext}/2$ where V_{ext} is the full opening rate. This material outflow is compensated by normal inflow V_b through the model base. The tangential stress is zero along the vertical and bottom boundaries, allowing for tangential motion. The top surface is a true free surface.

The surface temperature is kept constant at 0°C. The temperature at the bottom boundary is also fixed, at 1345°C. Lateral boundaries are thermally isolated. We prescribe an initial steady-state continental geotherm in the lithosphere, with an LAB temperature of 1300° and upper and lower crustal heat productions of 1 and 0.1 $\mu W/m^3$, respectively. In the asthenosphere an initial adiabatic temperature profile is prescribed based on an adiabatic surface temperature of ∼1284°C. Boundary condition for composition is fixed to initial composition along the top and bottom boundary.

A Gaussian-shaped lithosphere-asthenosphere thermal and compositional perturbation with an amplitude and standard deviation of 5 km and 10 km, respectively, helps localize deformation at the centre of the model. We randomly distributed heterogeneities around the rift axis throughout the whole depth of the model representing the pre-weakened lithosphere (Dyksterhuis et al., 2007). The magnitudes of these random perturbations of initial plastic strain follow a broad Gaussian envelope of 100 km standard deviation and a strain amplitude of 0.4. Strain weakening is implemented as a linear decrease in friction angle from 30° to 9° for brittle strain between 0 and 1. For plastic strains larger than 1, it remains constant at 9°. The choice of friction angle is based on the observations of the strength of the crust and faults in the MER (Muluneh et al., 2018). Plastic strain, defined as the second invariant of the deviatoric strain rate times the time step,

is tracked if the viscous stress exceeds the yield stress. For simplicity, cohesion is kept constant at a value of 20 MPa. All the rheological and thermal parameters as well as the ASPECT input file are given as supplementary material.

Numerical modeling of lithospheric extension can be conducted either through stress or kinematic boundary conditions (Brune et al., 2016). Since the opening of the MER is well documented by a number of geodetic and plate kinematic observations showing a relatively constant extension rate, we use the kinematic boundary condition. We run the model using a full opening rate of 6 mm/yr (Iaffaldano et al., 2014), leading to 66 km opening during the last 11 Myr. In order to assess the effect of different velocity boundary conditions, we also run the model using a 4 mm/yr constant opening rate (DeMets and Merkouriev, 2016) corresponding to the long term average during the last 16.5 Myr. Both models show similar deformation style at the end of model run. This implies that despite the difference in velocity boundary conditions, the deformation style is the same.

3.3 Model robustness and limitations

In order to validate the robustness of our results, we conducted additional models with viscosity cut-offs of 10^{18} and 10^{24} Pa s, which lead to almost indistinguishable results. We use time step of 5,000 years when applying the velocity of 6 mm/yr. Increasing or decreasing the time step by a factor of 2 does not change the results. Including linear cohesion softening did not significantly change the results.

Similar to previous modeling approaches, our experiment does not include the effect of a mantle plume, because the size of the studied plate boundary is in any case small compared to the extent of the African superplume (e.g., Nyblade et al., 2000). In addition, erosion, sedimentation, elasticity and magmatic underplating have not been implemented. Deformation in the MER is driven by constant, oblique kinematics since the onset of rifting at 11 Ma (e.g., Corti, 2008; DeMets and Merkouriev, 2016; Iaffaldano et al., 2014). We can not investigate the role of obliquity (Brune, 2014; Brune et al., 2012; Duclaux et al., 2019) or the impact of along-strike mantle flow (Mondy et al., 2018) due to the 2D nature of our experiment, but first order deformation aspects are nevertheless expected to be very well represented.

3.4 Model results

Our numerical experiment provides insight into deformation processes since the onset of rifting in MER. We discuss several outputs that are directly related to the seismogenic nature and strength of the crust.

3.4.1 Strain rate

At the beginning of deformation, strain is accommodated by small-scale shear zones controlled by the randomly distributed heterogeneities. Small-scale shear zones are active throughout the model domain until 2 Myr model time (Fig. 4A). The shear zones in upper and lower crust merge together and form a large offset border fault on the left side of the model that accommodates deformation until ~7 Myr. Further accommodation of deformation by this fault leads to significant thinning of the lower crust. Meanwhile synthetic and antithetic faults form on the right side of the rift. Between 7 and 9 Myr, significant thinning of the lower crust and strain migration from the border to rift floor faults occur. This occurs because the border fault on the left side rotates from high angles to low-angle, rendering mechanical activity unfeasible. At ~9 Myr model time, the maximum strain rate migrates from the border to the rift floor. At the end of model run (i.e. 11 Myr), there is a slight shift of the locus of deformation to the left side, similar to field observations in the rift (Ebinger and Casey, 2001). In general, our model evolves from asymmetric extension at the beginning of rifting to mostly symmetric rifting, generating a so-called asymmetric-symmetric pattern (Huismans and Beaumont, 2003). Figure 4A shows that the highest brittle strain rate (~2x10^{-14} s^{-1}) is accommodated by narrow conjugate faults distributed within a 30 km wide zone in the upper crust. These narrow, high strain rate zones accommodate the ongoing extension in the rift. Towards the base of the upper crust, high strain rate is widely distributed without forming narrow shear zones.

Outside the rift zone, high strain rate is observed at the base of the upper crust enhanced by shear deformation due to the rheological contrast between the upper and lower crust. The thickness of the upper crust remains constant throughout model evolution, while the lower crust has thinned significantly within the width of the rift zone leading to broadly distributed strain.

3.4.2 Brittle strain

Figure 4B indicates that time-integrated strain concentrates on the major fault on the left side since model initiation. As extension proceeds, the high angle fault rotates to very low dip angle in the lower crust where extension is broadly distributed. High angle shear zone penetrates to the base of lower crust and accumulates strain at depth by forming ramp-flat-ramp structure (Fig. 4B). In contrast, no significant strain accumulates on the right side of the rift until ~6 Myr model time. Soon after 6 Myr model time, faults on the right side start accommodating brittle extension together with faults on the left side until 11 Myr model time. In the rift floor and right-side of the model, deformation is mainly taken up by multiple, high angle faults with relatively small topographic offset.

3.4.3 Viscosity

Viscosity plots show the low-viscosity asthenospheric material and the presence of competent layers (Fig. 4C). Active shear zones in the upper crust and the whole lower crust are characterized by low effective viscosity ($<10^{21}$ Pa s). There is a slight deflection of the asthenospheric upwelling to the right guided by a high strain shear zone from the crust that forms a ramp-flat-ramp structure. The pattern of deflected asthenospheric upwelling is apparently similar to tomographic (Bastow et al., 2005) and magnetotelluric (e.g., Hübert et al., 2018) studies that show the offset of low-velocity anomalies away from the magmatic segments, although the clear pattern of the offset is difficult to explain due to the 2D nature of our numerical experiment. Similar deflection of asthenospheric upwelling and rift axis jump is also observed in previous numerical modeling experiments (Huismans and Beaumont, 2003; Tetreault and Buiter, 2018).

Available estimates of the vertically averaged viscosity in the EARS range from $10^{19.6}$ to 10^{23} Pa s (Stamps et al., 2014). Bendick et al. (2006) computed the viscoelastic relaxation effect following the 1993 dyking event in the northern MER. They found a best fit to observed displacement using a 15 km thick elastic/brittle crust over a viscous lower crust with viscosity of 1.125×10^{18} Pa s. Our lower crustal viscosity estimate is higher than that of Bendick et al. (2006). The difference could be due to the timescale of rapid dike injection and our modeling approach that considers the long-term deformation. High vis-

cosity in the lowermost part of the lower crust hints at possible brittle deformation and hence might explain lower crustal seismicity in MER (Lloyd et al., 2018).

3.4.4 Brittle and ductile layers

The occurrence of brittle deformation is assessed at each time step based on the Drucker-Prager yield criterion. Figure 4D shows the presence of brittle layers in the upper and lower crust and upper mantle. At the end of model run (11 Myr), the brittle layer in the lower crust is consumed and only ∼10 km thick brittle upper crust and ∼10 km thick upper mantle deform in brittle manner. Figure 4D also shows the occurrence of a brittle layer below 600 °C isotherm due to olivine dominated rheology of the upper mantle (McKenzie et al., 2005). Our numerical results at 11 Myr model time (Fig. 4D) also show that the crust is seismogenic both in the uppermost crust and in the deeper crust. The lower part of the upper crust and lower crust deforms in ductile manner.

3.5 Deviatoric stress

We explore the stress state arising from rift evolution and estimate the deviatoric stress that includes both the far-field and local components. Our model result offers a direct access to the stress tensor in 2D. The second invariant of the deviatoric stress in 2D is calculated using eqn. 9

$$\tau_{II} = \sqrt{\frac{1}{2}\tau_{ij}^2} = \sqrt{\frac{1}{2}(\tau_{xx}^2 + \tau_{yy}^2) + \tau_{xy}^2} \tag{9}$$

where τ_{xx}, τ_{yy}, τ_{xy} are the components of the deviatoric stress tensor.

Figure 5 shows that the boundary fault on the left side and ∼30 km depth on both left and right sides of the plateau are characterized by very high deviatoric stress (>∼200 MPa) whereas active shear zones in the upper crust and the lowermost crust are characterized by very low stress. The stress is more or less similar along the x-axis underneath the rift basin (Fig. 5) and therefore the precise location for the vertical section does not affect the discussion on the variation of stress with depth. The magnitude of stress increases from 20 MPa to 80 MPa in the upper most crust. From 8 km to 14 km depth, the stress decreases sharply to ∼10 MPa and then increases and reaches 160 MPa at ∼18 km before going back to 10 MPa at depth ≥30 km (Fig. 5).

4 Moment magnitude and earthquake b-value

We used the earthquakes from the EAGLE catalogue (Keir et al., 2006) to estimate the seismic moment release and b-values at different crustal depths. Seismic moment release (M_o) is the energy released by an individual earthquake and is a function of the earthquake's magnitude (Kanamori, 1983). The b-value describes the magnitude-frequency distribution of earthquakes, whereby a smaller value indicates a higher proportion of large earthquakes with respect to small earthquakes, and vice versa. Variations in the observed b-value have been attributed to changes in stress conditions and/or rock heterogeneity, and fluid diffusion (Marzocchi et al., 2020).

The calculation of seismic moment release (Fig. 6A &B) indicates that the majority of seismic moment release occurs in the upper crust above 8 km. A small seismic moment is released at depths of 8-14 km in the rift (Fig. 6B). We see a second peak in seismic moment release in the lower part of the upper crust at ∼16 km depth. Below this depth, seismic moment release is minimal. In order to obtain insight into the deformation style at different crustal depths and provide additional constrains to our modeling results, we estimate the b-value at depths ≤8 km, 8-14 km and ≥14 km. These depth ranges are selected based on the depth distribution of seismicity, occurrence of low-magnitude seismic swarms (Keir et al., 2006) and sharp increase in shear strength of faults (Muluneh et al., 2018). We calculate the magnitude of completeness (M_C) using the maximum curvature method (Wiemer and Wyss, 2000) that takes the magnitude 'bin' with the highest frequency and adds 0.2 magnitude units. We then use the maximum-likelihood calculation (Aki, 1965) and bootstrap analysis (Pickering et al., 1995) to calculate b-values and associated errors, respectively. The bootstrap analysis creates 10,000 datasets by randomly sampling the earthquake catalogue and allowing for duplication (supplementary figure 1), a b-value is calculated for each dataset and we report the mean and standard deviation of these values.

At depth shallower than 8 km, the b-value is 0.75±0.09 (466 earthquakes) and it increases to 0.91±0.06 (1059 earthquakes) at 8-14 km depth. The b-value decreases to 0.82±0.11 (396 earthquakes) below 14 km. The relatively higher b-value at 8-14 km coincides with increased number of earthquakes at ∼12 km (Keir et al., 2006) but due to a vast majority of earthquakes being relatively small in magnitude there is a small seismic moment release.

5 Comparison and discussion of results

We compare our numerical model results with observed deformation styles in the northern MER. Then, the brittleness of layers and stress from model results are compared with depth distribution of seismicity, b-value and crustal strength. We assume that no seismicity occurs where the applied stress is less than the yield strength (Scholz, 1988) and that geologically reasonable visco-plastic deformation represents the earthquake cycle that happens on a much shorter time scale.

We note that the crustal thickness from our model output differs from observations in the northern MER (Fig. 4&5). If we include the 5 km thick magmatic underplating (Maguire et al., 2006), the high deviatroic stress and brittle region will be within the crust, not the upper mantle, thus our model does not necessarily predict upper-mantle earthquakes. The thickness of the lower crust in our model represents only the upper ∼5 km of the lower crustal thickness inferred from geophysical observations (e.g., Maguire et al., 2006). Since most of the seismicity concentrates in the upper crust, the difference does not affect the discussion on the depth distribution of seismicity and model results.

5.1 Deformation style

Our 2D model successfully describes temporal deformation pattern in MER; including migration of high strain rate from border faults to 20-30 km wide segments, broadly distributed ductile extension in the lower part of the upper crust and in the lower crust and high accumulation of brittle strain on the border fault. The migration of high strain rate from the border faults to rift axis faults and magnitude of strain rate are comparable to GPS (e.g., Kogan et al., 2012), structural (Agostini et al., 2011) and modeling (Corti, 2008) observations in the northern MER. Strain migration occurs without the input from magma (Fig. 4A). Analogue modeling experiment shows that migration of strain from the border faults to magmatic segments does not necessarily require the input from magma, but can instead be caused by lithospheric thinning due to constant extensional kinematics (Corti, 2008).

The model results also indicate that brittle deformation occurs in two regions beneath the rift, in the uppermost crust and at the deeper crust. Deformation in the lowermost crust occurs in ∼70 km wide zone (Fig. 4A). Although our model result shows broadly distributed deformation in the lowermost crust, similar to field geophysical ob-

servations (Keranen et al., 2009; Kogan et al., 2012), the width of the deforming zone differs quite significantly. For example, Keranen et al. (2009) suggest that deformation in the lower part of the upper crust and lower crust is distributed in ∼400 km wide zone. On the other hand, Kogan et al. (2012) argue that deformation is localized in ∼85 km wide zone with some deformation extending outside the structural MER. In order to explain the widespread deformation, Keranen et al. (2009) argue that the lower crust must be weak. This contradicts with more recent modeling study suggesting that lower crust in MER must be strong in order to explain melt chemistry (Armitage et al., 2018).

5.2 Deviatoric stress and seismic moment release

In the EARS the magnitude of deviatoric stress is in a range of 10-20 MPa (Mahatsente and Coblentz, 2015; Stamps et al., 2010) and hence it appears to be too small to cause brittle failure on seismogenic faults (Craig et al., 2011; Scholz, 2002). Mahatsente and Coblentz (2015) argue that the ridge-push force from the oceanic part of Nubia (Africa)-Somalia plate is less than the integrated strength of the African plate and hence additional forces are required to deform the plate. The above studies report magnitude of vertically averaged deviatoric stress over the thickness of the lithosphere. Since both magnitude of deviatoric stress and strength vary with depth, detailed analysis on those parameters is crucial to understand the mechanism for the peak in mid crustal seismicity.

The second invariant of deviatoric stress in our models shows strong variation with depth. Figure 7 offers a clear representation of deviatoric stress and magnitude of seismic moment release with depth. The upper crust deforms with stress ranging from 20-80 MPa. This stress is higher than the shear strength of the upper crust, which is ∼20 MPa (Muluneh et al., 2018). A maximum of $\sim 1 \times 10^{15}$ Nm moment magnitude is released at 7 km depth. Between 8 and 14 km depth, the magnitude of stress decreases sharply to ∼10 MPa. The reduction in deviatoric stress is consistent with the observed occurrence of low-magnitude earthquake swarms with small seismic moment release and relatively higher b-value (Fig. 7). Alternatively we propose that earthquakes in the 8-14 km depth range, characterized by large numbers of small earthquakes, may be triggered by fluid release, potentially from cooling mafic intrusion (Keir et al., 2009). We observe a good correlation between the peak in seismic moment release at ∼16 km depth, and a peak to 160 MPa in the deviatoric stress in the lower part of the upper crust.

Figure 8 summarizes the distribution of seismicity and faults in the MER. The combination of high accumulated brittle strain and stress together with high seismic activity points out that the Ankober border fault and surrounding regions are still active and accommodate the present day opening of northern MER. Deformation at the rift centre is accommodated by active fault zones.

Previous studies from other sectors of the EARS (e.g., Albaric et al., 2009) show that the depth distribution of seismicity can be fitted to different yield strength envelopes depending on tectonic settings. Several lines of evidences suggest that deformation style and seismicity in the MER vary along (e.g., Déprez et al., 2013; Muluneh et al., 2017) and across the rift (Keranen et al., 2009; Kogan et al., 2012). Future studies should address the role of contrasting rheologies and thermal properties between the plateau and the rift in controlling the depth distribution of seismicity.

6 Conclusions

We present a detailed numerical modeling study of lithospheric extension and deviatoric stress state in the Main Ethiopian Rift (MER). Model results are compared with depth distribution of seismicity and seismic swarms, b-value and seismic moment release in order to propose a mechanism for deep crustal earthquakes in the MER. We use a high resolution, 2D numerical experiment to model the evolution of deformation and stress using most appropriate rheology for the lithosphere. Our model results successfully show the migration of deformation from border to rift centre, similar to GPS and geophysical observations. Analysis of the deviatoric stress based on model results show that stress significantly varies with depth in the MER floor. The uppermost crust (i.e. $\leq$8km) deforms with maximum stress of 80 MPa. The stress drops to 10 MPa at depth of 8-14 km and then increases to 160 MPa at $\sim$18 km. The peaks in stress correspond to peaks in seismic moment release in the MER crust. The low-stress depth range (i.e. 8-14 km) is characterized by ductile deformation, small seismic moment release, concentration of swarms of low-magnitude earthquakes and higher b-value. We conclude that the bimodal depth distribution of seismic moment release in the MER is controlled by the rheology of the deforming crust.

Acknowledgments

AM acknowledges the support from DFG under the TWAS-DFG cooperation visit to conduct the numerical modeling experiment at GFZ, Potsdam, Germany. SB and AG were funded through the Helmholtz Young Investigators Group CRYSTALS under Grant VH-NG-1132. FIK is funded by ECLIPSE Programme, which is funded by the New Zealand Ministry of Business, Innovation and Employment. This research is supported by the NERC through grant NE/L013932/1, and from Ministero Università e Ricerca (MiUR) through PRIN grant 2017P9AT72. The EAGLE earthquake data used in this paper can be found in Keir et al. (2006). Detailed and constructive reviews by Harro Schmeling and Patrice Rey greatly improved the manuscript. We thank the Computational Infrastructure for Geodynamics (CIG) for supporting the development of ASPECT, which is funded by the National Science Foundation under awards EAR-0949446 and EAR-1550901. Figures were drafted using Generic Mapping Tools (Wessel and Smith, 1998).

Software availability

The ASPECT plugins used in the manuscript is available here: https://zenodo.org/record/3758145#.Xp28CFDRZTY. The DOI is 10.5281/zenodo.3758145.

References

Agostini, A., Bonini, M., Corti, G., Sani, F., Manetti, P. (2011). Distribution of Quaternary deformation in the central Main Ethiopian Rift, East Africa. *Tectonics*, 30. https://doi:10.1029/2010TC002833.

Aki, K. (1965). Maximum likelihood estimate of b in the formula log (N)=a-bM and its confidence limit. *Bulletin of the Earthquake Research Institute, University of Tokyo*, 43, 237-239.

Albaric, J., Déverchère, J., Petit, C., Perrot, J., Le Gall, B. (2009). Crustal rheology and depth distribution of earthquakes: Insights from the central and southern east African Rift System. *Tectonophysics*, 468, 28 - 41.

Armitage, J.J., Petersen, K.D., Pérez-Gussinyé, M. (2018). The role of crustal strength in controlling magmatism and melt chemistry during rifting and break-up. *Geochemistry, Geophysics, Geosystems*, https://doi:10.1002/2017GC007326.

Bangerth, W., Dannberg, J., Gassmöller, R., Heister, T. (2018). ASPECT v2.0.0[software], doi:10.5281/zenodo.1244587, url: https://doi.org/10.5281/zenodo.1244587.

Bastow, I., Stuart, G.W., Kendall, J.-M., Ebinger, C.J. (2005). Upper-mantle seismic structure in a region of incipient continental breakup: Northern Ethiopian rift. *Geophysical Journal International*, 162(2), 479-493.

Behr, W.M., Platt, J.P. (2014). Brittle faults are weak, yet the ductile middle crust is strong: Implications for lithospheric mechanics. *Geophysical Research Letters*, 41, https://doi:10.1002/2014GL061349.

Bendick, R., McClusky, S., Bilham, R., Asfaw, L., Klemperer, S. (2006). Distributed Nubia-Somalia relative motion and dike intrusion. *Geophys. J. Int.* 165, https://doi:10.1111/j.1365246X.2006.02904.x.

van der Berg, A., van Keken, P., Yuen, D.A. (1993). The effects of a composite non-Newtonian and Newtonian rheology on mantle convection. *Geophysical Journal International*, 115, 62-78.

Beutel, E., van Wijk, J., Ebinger, C., Keir, D., Agostini, A. (2010). Formation and stability of magmatic segments in the Main Ethiopian and Afar rifts. *Earth and Planetary Science Letters*, 293, https://doi:10.1016/j.epsl.2010.02.006.

Bilham, R., Bendick, R., Larson, K., Mohr, P., Braun, J., Tesfaye, S., Asfaw, L. (1999). Secular and tidal strain across the Main Ethiopian Rift. *Geophysical Research Letter*, 26, 2789-2792.

Boccaletti, M., Bonini, M., Mazzuoli, R., Abebe, B., Piccardi, L., Tortorici, L. (1998). Quaternary oblique extensional tectonics in the Ethiopian Rift (Horn of Africa). *Tectonophysics*, 287, 97-116.

Brune, S. (2014). Evolution of stress and fault patterns in oblique rift systems: 3-D numerical lithospheric-scale experiments from rift to breakup. *Geochemistry, geophysics, Geosystems*, 15, https://doi:10.1002/2014GC005446.

Brune, S., Popov, A.A., Sobolev, S. (2012). Modeling suggests that oblique extension facilitates rifting and continental break-up. *Journal of Geophysical Research*, 117, https://doi:10.1029/2011JB008860.

Brune, S., Corti, G., Ranalli, G. (2017). Controls of inherited lithospheric heterogeneity on rift linkage: Numerical and analogue models of interaction between the Kenyan and Ethiopian rifts across the Turkana depression. *Tectonics*, https://doi:10.1002/2017TC004739.

Brune, S., Williams, S.E., Butterworth, N.P., Müller, D.R., 2016. Abrupt plate accelerations shape rifted continental margins. *Nature*, 1-4 https://doi.org/10.1038/nature18319.

Chambers, E.L., Harmon, N., Keir, D., Rychert, C. (2019). Using Ambient Noise to Image the Northern East African Rift. *Geochemistry, Geophysics, Geosystems,* https://doi: 10.1029/2018GC008129.

Corti, G. (2008). Control of rift obliquity on the evolution and segmentation of the Main Ethiopian Rift. *Nature Geosciences*, 1, 258–262.

Corti, G., Molin, P., Sembroni, A., Bastow, I.D., Keir, D. (2018). Control of pre-rift lithospheric structure on the architecture and evolution of continental rifts: Insights from the Main Ethiopian Rift, East Africa. *Tectonics*, 37, 477-496, https://doi.org/10.1002/2017TC004799.

Corti, G., Cioni, R., Franceschini, Z., Sani, F., Scaillet, S., Molin, P., Isola, I., Mazzarini, F., Brune, S., Keir, D., Erbello, A., Muluneh, A., Illsley-Kemp, F., Glerum, A.(2019). Aborted propagation of the Ethiopian rift caused by linkage with the Kenyan rift. *Nature communications*, https://doi.org/10.1038/s41467-019-09335-2.

Craig, T.J., Jackson, J.A., Priestley, K., McKenzie, D. (2011). Earthquake distribution patterns in Africa: their relationship to variations in lithospheric and geological structure, and their rheological implications. *Geophys. J. Int.* 185, 403-434.

Daly, E., Keir, D., Ebinger, C.J., Stuart, G.W., Bastow, I.D., Ayele, A. (2008). Crustal tomographic imaging of a transitional continental rift: the Ethiopian rift. *Geophys. J. Int.* 172, 1033-1048.

DeMets, C., Merkouriev, S. (2016). High-resolution estimates of Nubia-Somalia plate motion since 20 Ma from reconstructions of the Southwest Indian Ridge, Red Sea and Gulf of Aden. *Geophysical Journal International*, 207, 317-332.

Déprez, A., Doubre, C., Masson, F., Ulrich, P. (2013). Seismic and aseismic deformation along the East African Rift System from a reanalysis of the GPS velocity field of Africa. *Geophs. J. Int.* https://doi:10.1093/gji/ggt085.

Duclaux, G., Huismans, R.S., May, D.A. (2019). Rotation, narrowing, and preferential reactivation of brittle structures during oblique rifting. *Earth and Planetary Science Letters*, https://doi.org/10.1016/j.epsl.2019.115952.

Dyksterhuis, S., Rey, P., Muller, D., Moresi, L.-N. (2007). Effects of Initial weakness on rift architecture, in Imaging, Mapping and Modeling Continental Lithosphere Extension and Breakup. *edited by G. Karner, G. Manatschal, and L. D. Pinheiro, Geol. Soc. London Spec. Publ.* 282, 443-455.

Ebinger, C., Casey, M. (2001). Continental breakup in magmatic province. *Geology* 29, 527–530.

Fishwick, S. (2004). Surface wave tomography: Imaging of the lithosphere asthenosphere boundary beneath central and southern Africa? *Lithos*, 120, 63-73.

Glerum, A., Thieulot, C., Fraters, M., Blom, C., Spakman, W. (2018). Nonlinear viscoelasticity in ASPECT: benchmarking and applications to subduction. *Solid Earth*, 9, 267-294.

Glerum, A., Brune, S., Stamps, D. S., Strecker, M. R. (2020). Victoria continental microplate dynamics controlled by the lithospheric strength distribution of the East African Rift. *In press.* https://doi.org/10.1038/s41467-020-16176-x.

Greenfield, T., Keir, D., Kendall, J.-M., Ayele, A. (2019). Seismicity of the Bora-Tullu Moye volcanic field, 2016-2017. *Geochemistry, Geophysics, Geosystems*, 20, https://doi.org/10.1029/2018GC007648.

Hirth, G., Kohlstedt, D.L. (2003). Rheology of the upper mantle and the mantle wedge: a view from the experimentalists. *Geophys. Monogr.* 138, 83-105.

Heister, T., Dannberg, J., Gassmöller, R., Bangerth, W. (2017). High accuracy mantle simulation through modern numerical methods - II: realistic models and problems. *Geophysical Journal International* 210, 833-851.

Hofstetter, R., Beyth, M. (2003). The Afar Depression: interpretation of the 1960-2000 earthquakes. *Geophysical Journal International* 155, 715–732.

Hübert, J., Whaler, K., Fisseha, S. (2018). The electrical structure of the central Main Ethiopian Rift as imaged by magnetotellurics: implications for magma storage and pathways. *Journal of Geophysical Research: Solid Earth* 123, 6019-6032.

Huismans, R.S., Beaumont, C. (2003). Symmetric and asymmetric lithospheric extension: relative effects of frictional-plastic and viscous strain softening. *Journal of Geophysical Research*, http://dx.doi.org/10.1029/2002JB002026.

Iaffaldano, G., Hawkins, R., Sambridge, M. (2014). Bayesian noise-reduction in Arabia/Somalia and Nubia/Arabia finite rotations since 20 Ma: Implications for Nubia/Somalia relative motion. *Geochem. Geophys. Geosyst.*, 15, https://doi:10.1002/2013GC005089.

Karato, S., Wu, P. (1993). Rheology of the upper mantle: A synthesis. *Science*, 260, 771-778.

Kazmin, V., Berhe, SM. (1981). Geological map of the Ethiopian Rift. *Geological Survey of Ethiopia, Ministry of Mines*, Addis Ababa.

Kanamori, H. (1983). Magnitude scale and quantification of earthquakes. *Tectonophysics*, 93, https://doi.org/10.1016/0040-1951(83)90273-1.

Keir, D., Bastow, I.D., Whaler, K.A., Daly, E., Cornwell, D.G., Hautot, S. (2009). Lower crustal earthquakes near the Ethiopian rift induced by magmatic processes. *Geochemistry, Geophysics, Geosystems*, 10, https://doi:10.1029/2009GC002382.

Keir, D., Ebinger, C., Stuart, G., Daly, E., Ayele, A. (2006). Strain accomodation by magmatism and faulting as rifting proceeds to breakup: seismicity of the northern Ethiopian Rift. *Journal of Geophysical Research*, 111, https://doi:10.1029/2005jb003748.

Keranen, K., Klemperer, S., Gloaguen, R., EAGLE working group. (2004). Three-dimensional seismic imaging of a protoridge axis in the Main Ethiopian rift. *Geology*, 32, https://doi:10.1130/G20737.1.

Keranen, K., Klemperer, S., Julia, J., Lawrence, J., Nyblade, A. (2009). Low lower crustal velocity across Ethiopia: Is the Main Ethiopian Rift a narrow rift in a hot carton? *Geochemistry, Geophysics, Geosystem*, 10. https://doi:10.1029/2008GC002293.

Kogan, L., Fisseha, S., Bendick, R., Reilinger, R., McClusky, S., King, R., Solomon, T. (2012). Lithospheric strength and strain localization in continental extension from observations of the East African Rift. *Journal of Geophysical Research*, 117, https://doi:10.1029/2011JB008516.

Kronbichler, M., Heister, T., Bangerth, W. (2012). High accuracy mantle convection simulation through modern numerical methods. *Geophysical Journal International*, 191, 12-29.

Kurz, T., Gloaguen, R., Ebinger, C., Casey, M., Abebe, B. (2007). Deformation distribution and type in Main Ethiopian Rift MER: a remote sensing study. *Journal of African Earth Sciences*, 48, 100–114.

Lavayssière, A., Drooff, C., Ebinger, C., Gallacher, R., Illsley-Kemp, F., Oliva, S.J., Keir, D. (2019). Depth extent and kinematics of faulting in the southern Tanganyika Rift, Africa. *Tectonics*, 38, 842-862.

Lavecchia, A., Beekman, F., Clark, S.R., Cloetingh, S.A.P.L. (2016). Thermo-rheological aspects of crustal evolution during continental breakup and melt intrusion: The main Ethiopian Rift, East Africa. *Tectonophysics*, 686, 51-62.

Lindenfeld, M., Rümpker, G., Link, K., Koehn, D., Batte, A. (2012). Fluid-triggered earthquake swarms in the Rwenzori region, East African Rift- Evidence for rift initiation. *Tectonophysics*, 566, 95-104.

Lloyd, R., Biggs, J., Wilks, M., Nowacki, A.,Kendall, J-M., Ayele, A., Lewi, E., Eysteinsson, H. (2018). Evidence for cross rift structural control on deformation and seismicity at a continental rift caldera. *Earth and Planetary Science Letters*, 487, 195-200.

Mackenzie, D., Thybo, H., Maguire, P. (2005). Crustal velocity structure across the Main Ethiopian Rift: Results from 2-dimensional wide-angle seismic modeling. *Geophys. J. Int.*, 162, 996-1006.

Maguire, P.K.H., Keller, G.R., Klemperer, S.L., Mackenzie, G.D., Keranen, K., Harder, S., O'Reilly, B., Thybo, H., Asfaw, L., Khan, M.A., Amha, M. (2006). Crustal structure of the northern Main Ethiopian Rift from the EAGLE controlled-source surveys; a snapshot of incipient lithospheric break-up. In: Yirgu, G., Ebinger, C. and Maguire, P.K.H. eds., The Afar volcanic province within the East African Rift System: *Geological Society of London*, 259, 269-291.

Mahatsente, R., Coblentz, D. (2015). Ridge-push force and the state of stress in the Nubia- Somalia plate system. *Lithosphere*, 7, https://doi:10.1130/L441.1.

Marzocchi, W., Spassiani, I., Stallone, A., Taroni, M. (2020). How to be fooled searching for significant variations of the b-value. *Geophysical Journal International*, 220, 1845-1856, https://doi.org/10.1093/gji/ggz541.

McKenzie, D., Jackson, J., Priestley, K. (2005). Thermal structure of oceanic and continental lithosphere. *Earth and Planetary Science Letters*, 233, 337-349.

Mondy, W., Rey, P.F., Duclaux, G., Moresi, L., (2018). The role of asthenospheric flow during rift propagation and breakup. *Geology*, 46, 103 - 106, https://doi.org/10.1130/G39674.1.

Muluneh, A., Cuffaro, M., Kidane, T. (2017). Along-strike variation in deformation style inferred from kinematic reconstruction and strain rate analysis: A case study of the Ethiopian Rift. *Phys. Earth Planet. Inter.*, 270, 176 - 182, http://dx.doi.org/10.1016/j.pepi.2017.07.009.

Muluneh, A., Kidane, T., Corti, G., Keir, D. (2018). Constraints on fault and crustal strength of the Main Ethiopian Rift from formal inversion of earthquake focal mechanism data. *Tectonophysics*, 731-732, 172-180.

Naliboff, J. B., Glerum, A., Brune, S., Peron-Pinvidic, G., Wrona, T. (2020). Development of 3D rift heterogeneity through fault network evolution. *Geophysical Research Letters*. https://doi.org/10.1029/2019GL086611.

Nyblade, A.A., Owens, T.J., Gurrola, H., Ritsema, J., Langston, C.A. (2000). Seismic evidence for a deep upper mantle thermal anomaly beneath east Africa. *Geology*, 28, 599-602.

Pickering, G., Bull, J.M., Sanderson, D.J. (1997). Minimum Magnitude of Completeness in Earthquake Catalogs: Examples from Alaska, the Western United States, and Japan. *Bulletin of the Seismological Society of America*, 262,

90,859-869,

Rose, I., Buffett, B., Heister, T. (2017). Stability and accuracy of free surface time integration in viscous flows. *Physics of Earth and Planetary Interiors*, 262, 90-100.

Rutter, E.H., Brodie, K.H. (2004). Experimental grain size-sensitive flow of hot-pressed Brazilian quartz aggregates. *Journal of Structural Geology*, 26, 2011-2023.

Rybacki, E., Gottschalk, M., Wirth, R., Dresen, G. (2006). Influence of water fugacity and activation volume on the flow properties of fine-grained anorthite aggregates. *Journal of Geophysical Research*. 111, B03203.

Saria, E., Calais, E., Stamps, D.S., Delvaux, D., Hartnady, C.J.H., (2014). Present-day kinematics of the East African Rift. *Journal of Geophysical Research*, 119, 3584-3600.

Scholz, C.H. (1988). The brittle-plastic transition and the depth of seismic faulting. *Geologische Rundschau*, 77/1, 319-328.

Scholz, C.H. (2002). The mechanics of earthquakes and faulting. Cambridge University Press. 2nd edition.

Seno, T., Saito, A. (1994). Recent East African earthquakes in the lower crust. *Earth Planet. Sci. Lett.*, 121, 125 - 136.

Stamps, D.S., Flesch, L.M., Calais, E. (2010). Lithospheric buoyancy forces in Africa from a thin sheet approach. *Int J Earth Sci*, https://doi:10.1007/s00531-010-0533-2.

Stamps, D.S., Flesch, L.M., Calais, E., Ghosh, A. (2014). Current kinematics and dynamics of Africa and the East African Rift System. *Journal of Geophysical Research* 119, https://doi:10.1002/2013JB010717.

Tetreault, J.L., Buiter, S.J.H. (2018). The influence of extension rate and crustal rheology on the evolution of passive margins from rifting to break-up. *Tectonophysics*, 746, 155-172.

Wessel, P., Smith, W. (1998). New, improved version of the Generic Mapping Tools released. *EOS Trans. AGU* 79, 579.

Wilks, M., Kendall, J-M., Nowacki, A., Biggs, J., Wookey, J., Birhanu, Y., Ayele, A., Bedada, T. (2017). Seismicity associated with magmatism, faulting and hydrothermal circulation at Aluto Volcano, Main

687 Ethiopian Rift. *Journal of Volcanology and Geothermal Research*,
688 https://doi:10.1016/j.jvolgeores.2017.04.003.
689 Wiemer, S., Wyss, M. (2000). Minimum magnitude of completeness in earth-
690 quake catalogs: Examples from Alaska, the Western United States and
691 Japan. *Bulletin of the Seismological Society of America*, 90, 859-869,
692 https://doi.org/10.1785/0119990114.
693 Wolfenden, E., Ebinger, C., Yirgu, G., Deino, A., Ayalew, D. (2004). Evolution of
694 the northern Main Ethiopian Rift: birth of a triple junction. *Earth and Plane-*
695 *tary Science Letters*, 224, 213–228.
696 Yang, Z., Chen, W-P. (2010). Earthquakes along the East African Rift Sys-
697 tem: A multi scale, system-wide perspective. *J. Geophys. Res.*, 115,
698 https://doi:10.1029/2009JB006779.

699 ## Figure captions

Figure 1. Location of the Main Ethiopian Rift. Earthquake focal mechanisms are compiled from Hofstetter and Beyth (2003); Keir et al. (2006). GPS velocity vector shows the motion of Somalia with respect to Africa (Nubia) (Iaffaldano et al., 2014, similar to Saria et al. 2014 for the rigid zones). The red triangles are active volcanoes from the Smithsonian Institution, Global Volcanism Program (https://volcano.si.edu). The open black box shows the location of Fig. 2A and the open white box on the inset map shows the location of the main map. Elevation data is taken from GEBCO database (https://www.gebco.net).

Figure 2. (A) Earthquakes in the Main Ethiopian Rift from EAGLE dataset (Keir et al., 2006) scaled to their magnitudes and colored with hypocentral depth. The polygons bound earthquakes that occur in the plateau and rift floor. Thin gray lines indicate faults in the rift (e.g., Boccaletti et al., 1998; Kazmin and Berhe, 1981). AA′ and BB′ profile lines show earthquake hypocentres depicted in the middle and bottom figures, respectively. The profiles project earthquakes within 20 km of the line in the northern and central MER. (B) seismicity continues to ∼32 km whereas in (C) seismicity is concentrated in the upper ∼12 km (i.e. by considering the hypocentral uncertainty of ±2 km).

Figure 3. Model geometry and boundary conditions. V_{ext} is horizontal, full spreading rate of opening that drives extension and V_b at the model base balances material outflow. A mechanically weak heterogeneity at the base of the lithosphere helps localize deformation at the centre. We run the model for 11 Myr leading to 66 km extension, which is within the range of predicted extension for the northern MER. The dashed black box shows the subset (200km×60km) of total domain of the model discussed in figs. 4 and 5.

Figure 4. Snapshots of strain rate (A), accumulated strain (B), viscosity (C) and deformation type (D) at 3, 9 and 11 Myr. At 3 Myr, deformation localized on the major fault on the left side. Similar to strain rate map (A), strain began to accumulate on the left side marginal fault. As extension proceeds, the marginal fault on the left side rotates to become horizontal (B). Since 9 Myr, deformation migrates from the rift border to the centre. At 11 Myr, active deformation with maximum strain rate is localized into ∼30 km wide zone. High strain rate in the middle and lower crust indicates that deformation is mainly accommodated by broadly distributed flow instead of focusing of strain on active shear zones. The viscosity map (C) indicates the evolution of strong and weak zones. The lower part of the upper crust at 11 Myr is the weakest with viscosity less than 10^{21} Pa s and characterized by ductile deformation (D). The brittle layer in the lower crust at the beginning of deformation is consumed during rifting (D). The white lines in all figures show temperature contours in °C.

Figure 5. Map showing the magnitude of the second invariant of the deviatoric stress at 11 Myr model time corresponding to present-day. The middle crust and active shear zones in the uppermost crust are characterized by very low deviatoric stress. Maximum stress is observed along the western rift border fault and beneath the western and eastern plateaus. The white line at the centre of the figure depicts the location for the vertical section shown in Fig. 7. The contours show the magnitude of deviatoric stress at 50 MPa interval.

Figure 6. The sum of seismic moment release in 1 km depth bins estimated using the relationship M_0=$10^{\frac{3}{2}M_w+9.1}$ Nm for plateau (A) and rift (B) shown by regions bounded by thick polygon. We make assumption that $M_L = M_w$. The red bars indicate the seismic moment released by low-magnitude earthquake swarms (Keir et al., 2006).

Figure 7. Seismic moment release, variation of magnitude of deviatoric stress with depth at the centre of the rift (Fig. 5) and earthquake b-value. Low stress region coincides with swarms of low-magnitude earthquake in the rift zone, small seismic moment release (red bars) and relatively higher b-value. Note that this layer has a shear strength ranging from ∼40 to ∼120 MPa (Muluneh et al., 2018, similar to global compilation of shear stresses from major boundary faults by Behr and Platt (2014)). The green lines indicate the depth ranges ($\leq$8 km, 8-14 km, $\geq$14 km) at which b-values are estimated.

Figure 8. Schematic cross-section across the northern MER from NW to SE. Earthquakes are also projected along the same profile line. Black lines show the interpreted major faults while the red lines show the minor faults within the rift axis. The dashed red line indicates the depth to the Moho (e.g., Keranen et al., 2009). The pattern and geometry of faults are similar to our modeled brittle strain at 11 Myr model time (Fig. 4B). The geology of the section is modified after Corti et al. (2018, and references therein).

Figure 1.

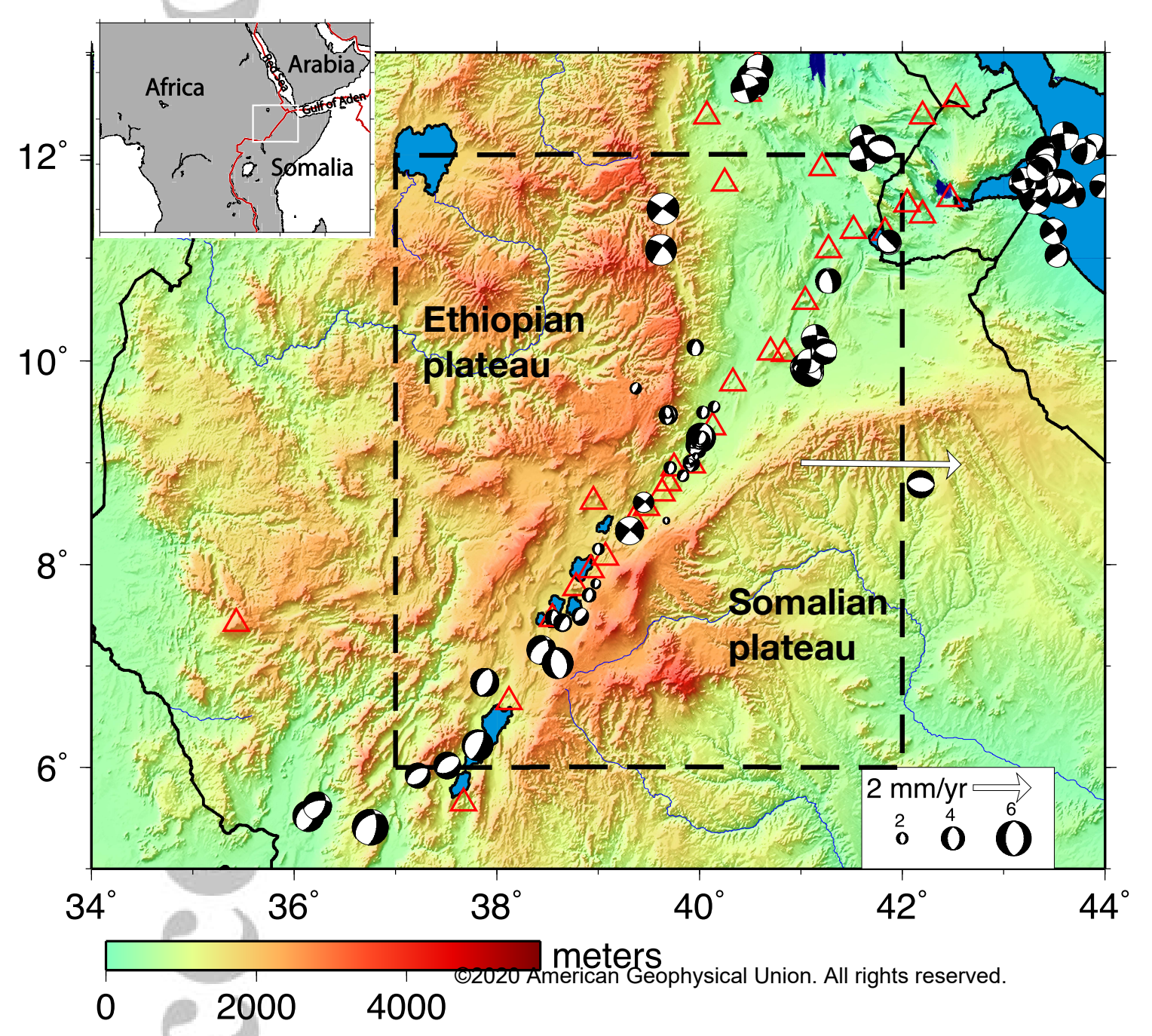

Figure 2.

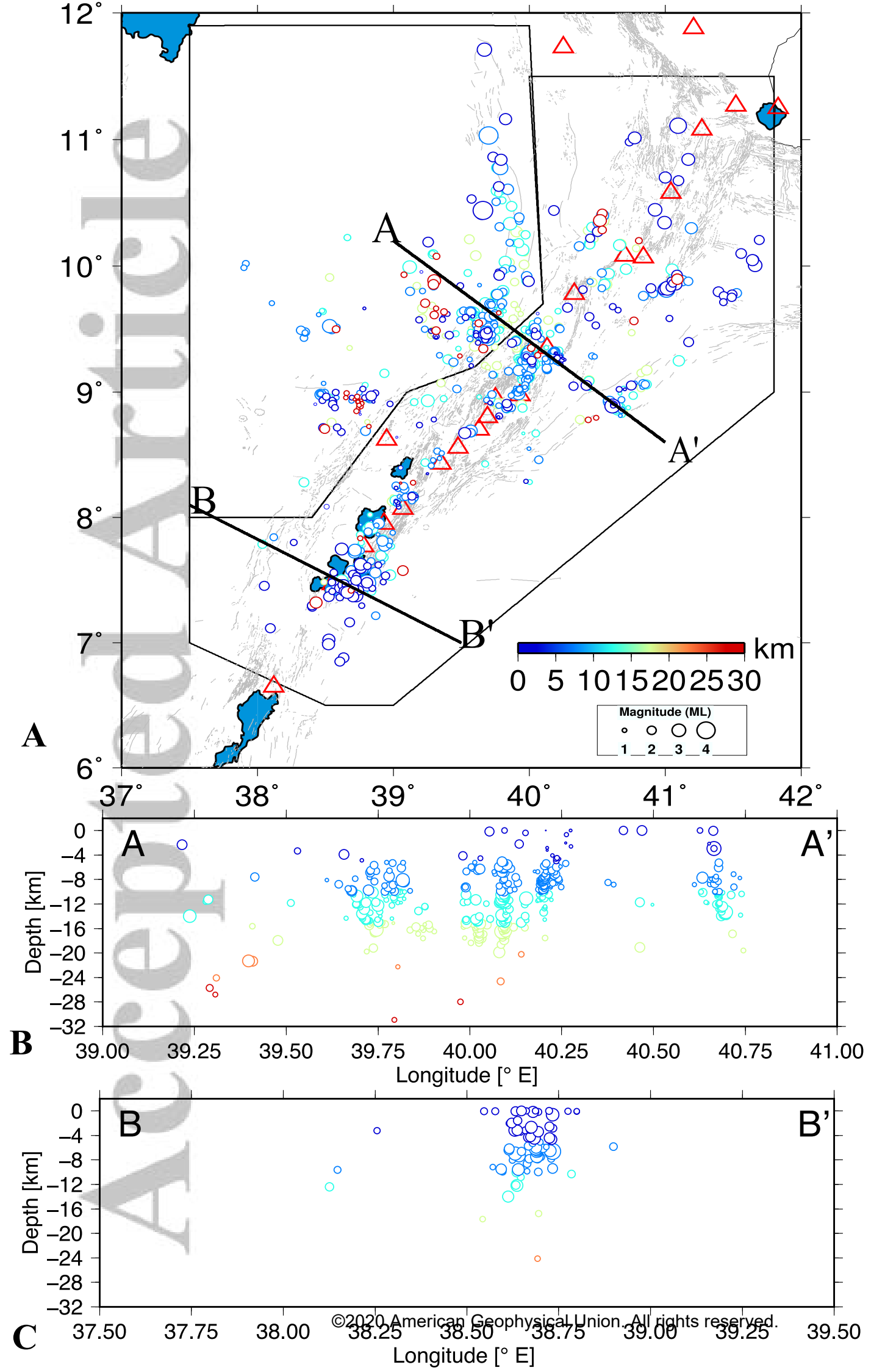

Figure 3.

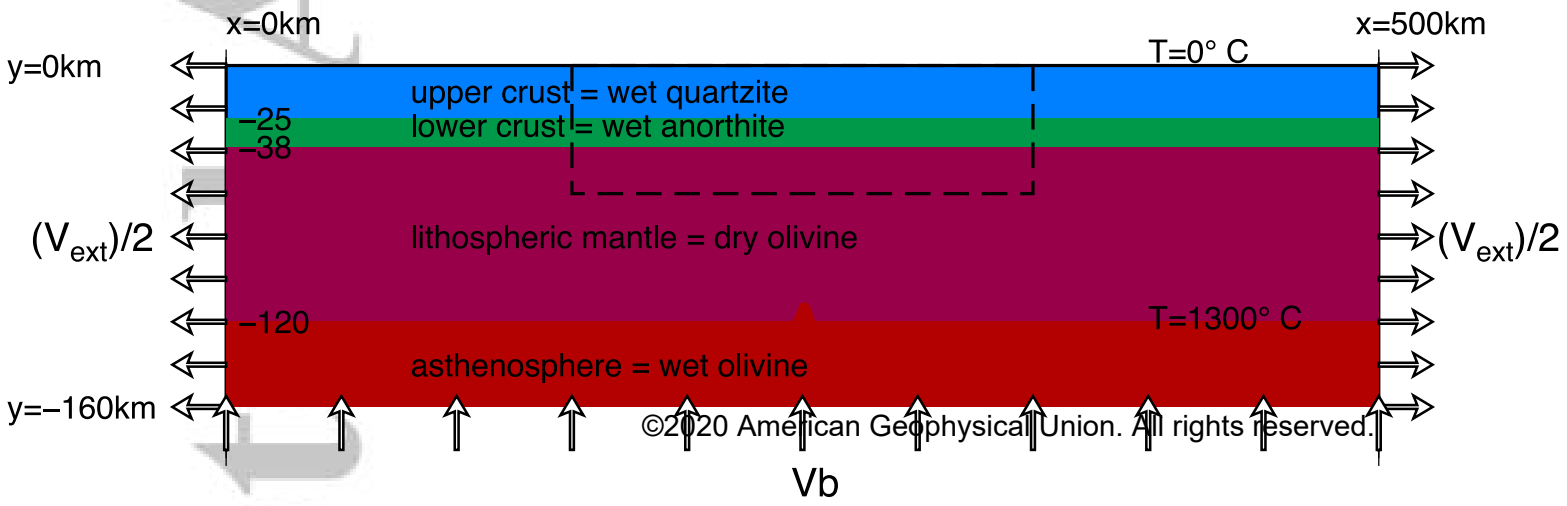

Figure 4.

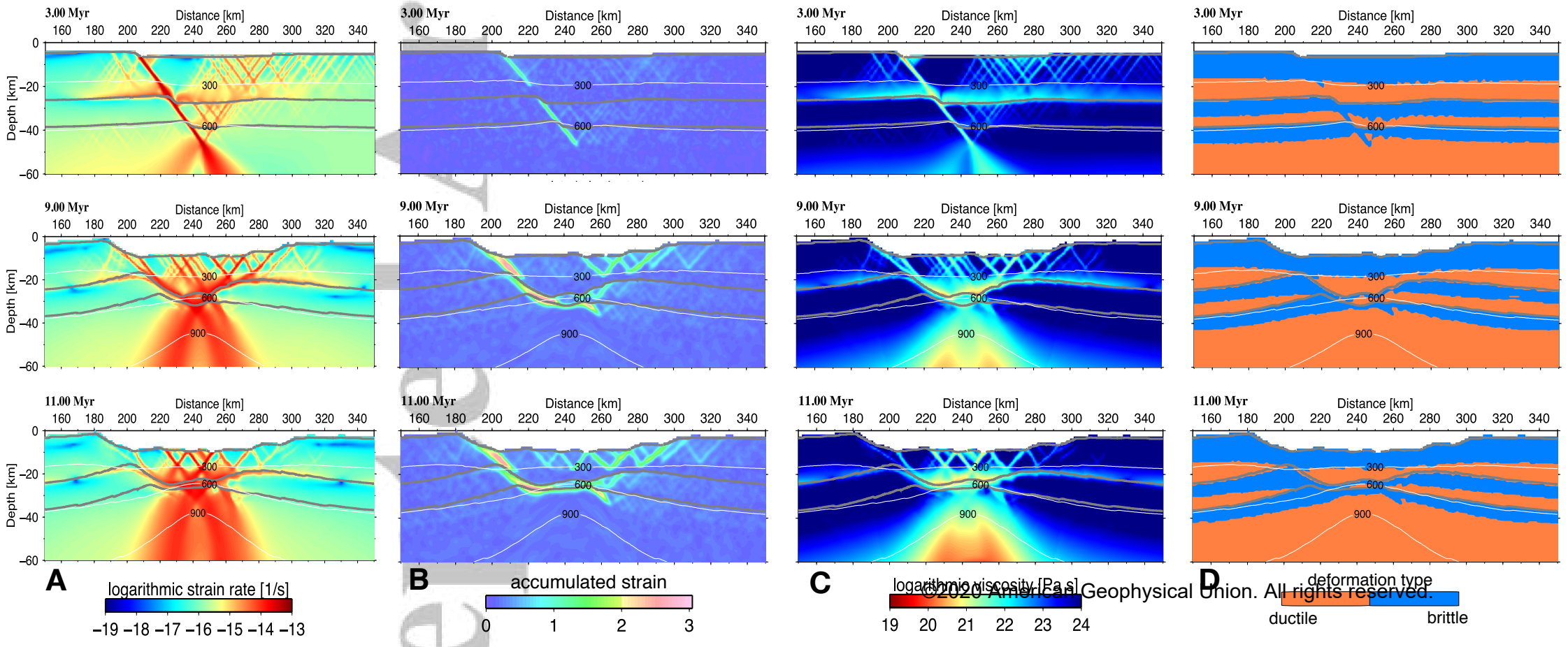

Figure 5.

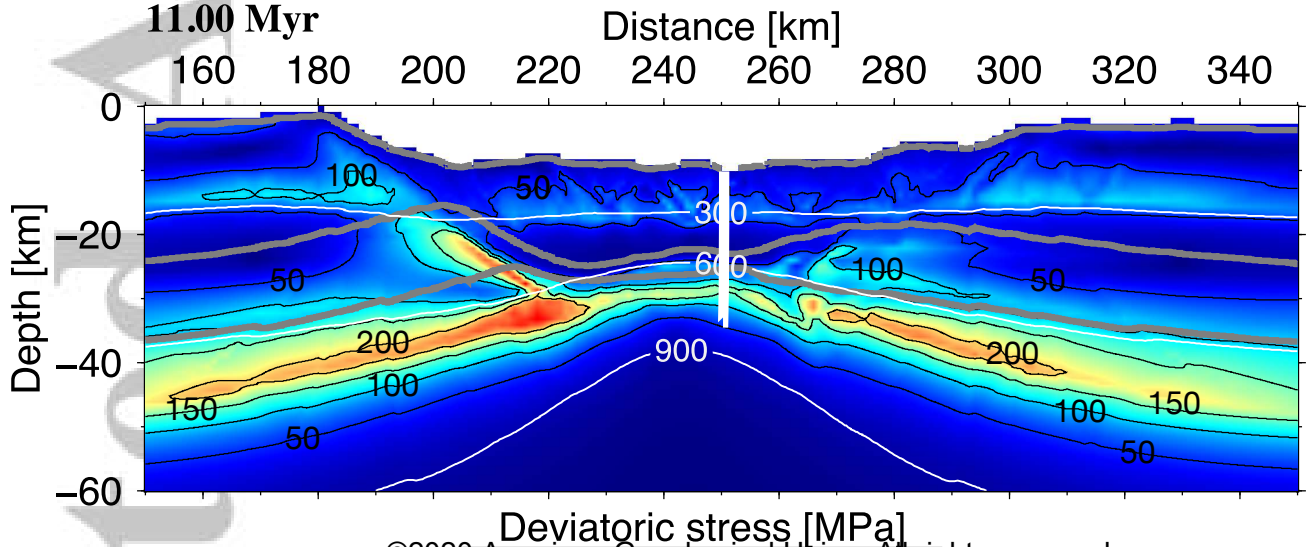

Figure 6.

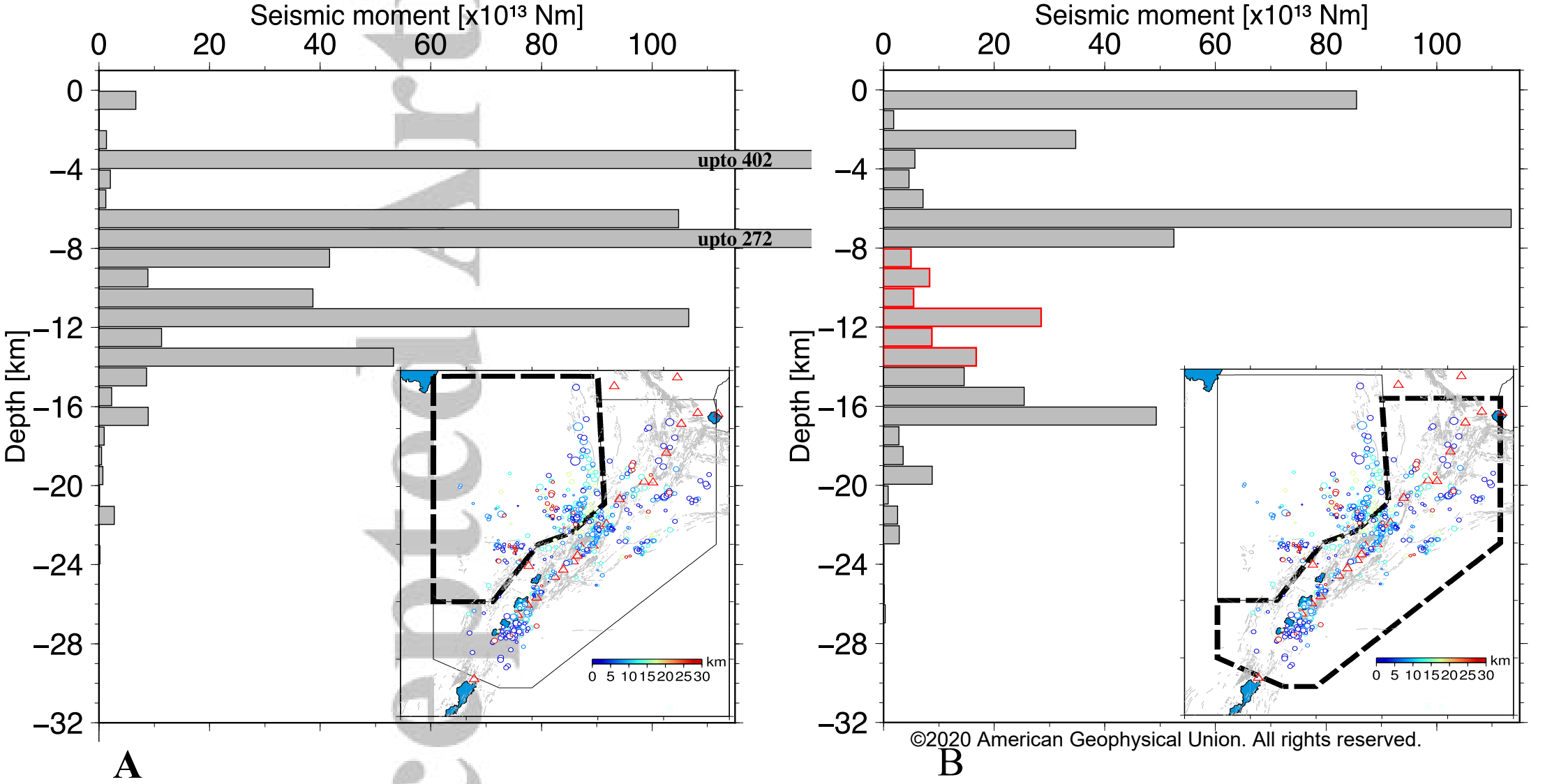

Figure 7.

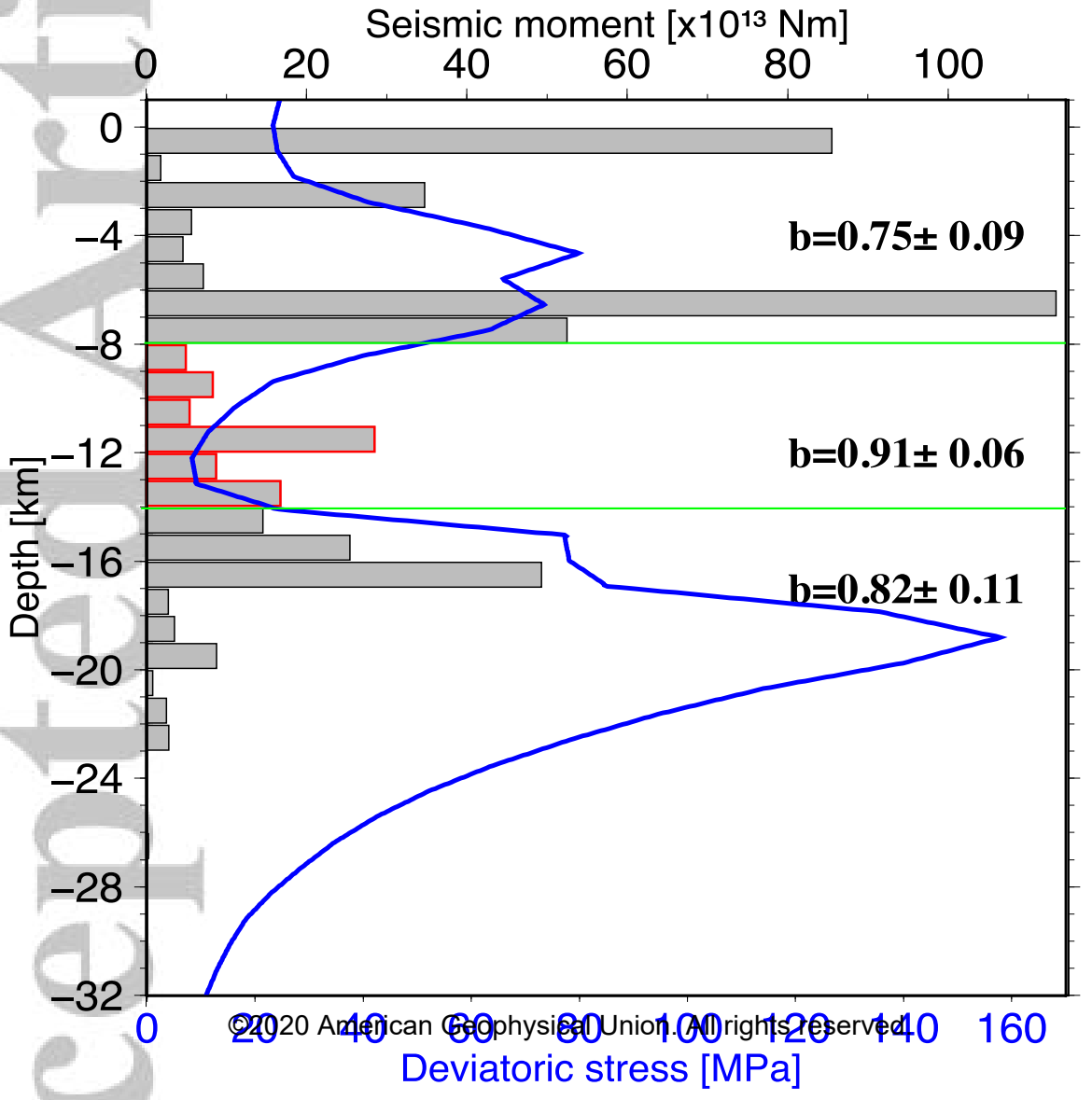

Figure 8.